Mon. Not. R. Astron. Soc. **395,** 1999–2012 (2009) doi:10.1111/j.1365-2966.2009.14715.x

High-energy particle acceleration at the radio-lobe shock of Centaurus A

J. H. Croston,[1⋆] R. P. Kraft,[2] M. J. Hardcastle,[1] M. Birkinshaw,[2,3] D. M. Worrall,[2,3] P. E. J. Nulsen,[2] R. F. Penna,[2] G. R. Sivakoff,[4,5] A. Jordán,[2,6] N. J. Brassington,[2] D. A. Evans,[2,7] W. R. Forman,[2] M. Gilfanov,[8,9] J. L. Goodger,[1] W. E. Harris,[10] C. Jones,[2] A. M. Juett,[11] S. S. Murray,[2] S. Raychaudhury,[12] C. L. Sarazin,[4] R. Voss[8,13] and K. A. Woodley[10]

[1]*School of Physics, Astronomy and Mathematics, University of Hertfordshire, College Lane, Hatfield, Hertfordshire AL10 9AB*
[2]*Harvard-Smithsonian Center for Astrophysics, 60 Garden Street, Cambridge, MA 02138, USA*
[3]*H. H. Wills Physics Laboratory, University of Bristol, Tyndall Avenue, Bristol BS8 1TL*
[4]*Department of Astronomy, University of Virginia, PO Box 400325, Charlottesville, VA, 22904-4325, USA*
[5]*Department of Astronomy, 4055 McPherson Laboratory, Ohio State University, 140 West 18th Avenue, Columbus, OH*
[6]*Departamento de Astronomía y Astrofísica, Pontificia Universidad Católica de Chile, Casilla 306, Santiago 22, Chile*
[7]*Massachusetts Institute of Technology, Kavli Institute for Astrophysics and Space Research, 77 Massachusetts Avenue, Cambridge, MA 02139, USA*
[8]*Max-Planck-Institut für extraterrestrische Physik, Giessenbackstrasse, D-85748, Garching, Germany*
[9]*Space Research Institute, Russian Academy of Sciences, Profsoyuznaya 84/32, 117997 Moscow, Russia*
[10]*Department of Physics and Astronomy, McMaster University, Hamilton, ON L8S 4M1, Canada*
[11]*Laboratory for X-Ray Astrophysics, NASA Goddard Space Flight Center, Greenbelt, MD 20771*
[12]*School of Physics and Astronomy, University of Birmingham, Edgbaston, Birmingham B15 2TT*
[13]*Excellence Cluster Universe, Technische Universität München, Boltzmannstr. 2, D-85748, Garching, Germany*

Accepted 2009 February 27. Received 2009 February 19; in original form 2009 January 9

ABSTRACT

We present new results on the shock around the south-west radio lobe of Centaurus A using data from the *Chandra* Very Large Programme observations (740 ks total observing time). The X-ray spectrum of the emission around the outer south-western edge of the lobe is well described by a single power-law model with Galactic absorption – thermal models are strongly disfavoured, except in the region closest to the nucleus. We conclude that a significant fraction of the X-ray emission around the south-west part of the lobe is synchrotron, not thermal. We infer that in the region where the shock is strongest and the ambient gas density lowest, the inflation of the lobe is accelerating particles to X-ray synchrotron emitting energies, similar to supernova remnants such as SN1006. This interpretation resolves a problem of our earlier, purely thermal, interpretation for this emission, namely that the density compression across the shock was required to be much larger than the theoretically expected factor of 4. We describe a self-consistent model for the lobe dynamics and shock properties using the shell of thermal emission to the north of the lobe to estimate the lobe pressure. Based on this model, we estimate that the lobe is expanding to the south-west with a velocity of $\sim$2600 km s^{-1}, roughly Mach 8 relative to the ambient medium. We discuss the spatial variation of spectral index across the shock region, concluding that our observations constrain $\gamma_{\rm max}$ for the accelerated particles to be $\sim 10^8$ at the strongest part of the shock, consistent with expectations from diffusive shock acceleration theory. Finally, we consider the implications of these results for the production of ultra-high energy cosmic rays (UHECRs) and TeV emission from Centaurus A, concluding that the shock front region is unlikely to be a significant source of UHECRs, but that TeV emission from this region is expected at levels comparable to current limits at TeV energies, for plausible assumed magnetic field strengths.

⋆E-mail: J. H.Croston@herts.ac.uk

Key words: shock waves – galaxies: active – galaxies: elliptical and lenticular: cD – galaxies: individual: Cen A – radio continuum: galaxies – X-rays: galaxies.

1 INTRODUCTION

The mechanisms by which radio-loud active galaxies transfer energy to their surroundings are of considerable interest, due to the likely role of such energy input in counteracting gas cooling in the central regions of galaxies, galaxy groups and clusters. Shocks are particularly important, as they provide a means of increasing the entropy of the surrounding gas. There are now a number of examples of shocks associated with radio galaxies, which include weak shock structures in the intracluster medium (ICM) of some of the nearest galaxy clusters (e.g. Fabian et al. 2003, 2006; Forman et al. 2005) generally on scales larger than the radio lobes, and a small number of examples of strong shocks associated with galaxy-scale radio lobes in comparatively isolated environments (e.g. Kraft et al. 2003, 2007a; Croston, Kraft & Hardcastle 2007; Jetha et al. 2008).

The best-studied example of a strong shock associated with a radio galaxy is the prominent shell of bright X-ray emission surrounding the south-west inner lobe of Centaurus A (Cen A), detected with *Chandra* and *XMM–Newton*, as first reported by Kraft et al. (2003). As Cen A (NGC 5128) is the nearest radio galaxy ($D_L = 3.7$ Mpc, see below), it is an ideal laboratory for investigating the physics of radio-lobe shocks and their effects on the galaxy interstellar medium (ISM). Kraft et al. (2003) interpreted the bright X-ray emission as thermal in origin, based on acceptable fits to a thermal spectrum, and a lack of radio emission at the location of the shock front (as might be expected if the X-ray emission was associated with high-energy particle acceleration); however, their analysis raised questions about the shock hydrodynamics, as the apparent density contrast between shocked and unshocked material was significantly higher than the expected value of 4 for a strong shock (where the adiabatic index is 5/3). In Kraft et al. (2007a), deeper *Chandra* observations were used to resolve the structure of the shock front in more detail, and to investigate the shock structure as a function of position. They developed a more complex two-fluid model for the shocked material, which accommodated the electrons and ions in the shocked material being out of equilibrium. However, that work did not address the issue of the density contrast between pre-shocked and post-shocked gas.

Here, we present a new analysis of the Cen A shock properties, based on very deep *Chandra* observations of the source as part of a Very Large Programme carried out in *Chandra* Cycle 9. A total of ∼740 ks of *Chandra* data on Cen A is now available by combining all of the available *Chandra* data. This rich data set has already been used to carry out detailed studies of the X-ray binary population in NGC 5128 (Jordán et al. 2007; Sivakoff et al. 2008), particle acceleration in the X-ray jet (Hardcastle et al. 2007; Worrall et al. 2008) and of the galaxy ISM (Kraft et al. 2008). Our analysis in this paper of the new deep observations of the Cen A shell revises some of the conclusions of earlier work by Kraft et al.

In Section 2, we summarize the data reduction and analysis. In Section 3, we discuss the results of our new spatial and spectral analysis of the X-ray shell, and in Section 4 we compare our results with previous work, present a new interpretation for the majority of the shell X-ray emission, and discuss the implications of that interpretation. We adopt a distance of 3.7 Mpc to Cen A (the average of five distance estimates to Cen A – see section 6 of Ferrarese et al. 2007), giving an angular scale of 1 arcsec = 17.9 pc.

2 DATA PREPARATION AND ANALYSIS

Cen A has now been observed a total of 10 times using *Chandra*'s AXAF CCD Imaging Spectrometer (ACIS) instrument. The south-west radio lobe and surrounding X-ray shell are entirely within the detector area for seven of these observations (ObsIDs 0962, 2978, 3965, 7797, 7800, 8489 and 8490). The effective on-source time for the entire shell region is ∼507 ks. The inner parts of the shell have a higher total exposure time, but for this analysis we chose to include only the data sets in which the entire shell falls within the detector field of view. The data sets were all processed uniformly using CIAO version 3.4 and CALDB version 3.3.0.1. Further details of the data processing are given in Sivakoff et al. (2008) and Hardcastle et al. (2007). Spectral fitting was carried out using XSPEC.

Since the primary beam of the Very Large Array (VLA) limits the sensitivity of maps of Cen A at high frequencies and large distances from the pointing centre, we made a new radio map with an effective frequency of 1.5 GHz from archival VLA data sets. We combined data from observations with the VLA in its A configuration (AB257: 1983 October 30), B configuration (AC175: 1986 August 11), BnC configuration (AC175: 1986 Oct 03) and CnD configuration (AB587: 1991 February 16) to give a map that had the highest possible resolution while sampling the large-scale structure to the extent possible with the VLA at this frequency. Calibration and data reduction were carried out with AIPS in the standard way. The resulting map has a resolution of 6.1×1.9 arcsec^2 [full width at half-maximum (FWHM) of major and minor axes of elliptical Gaussian: the major axis is closely aligned with the north-south axis] and is dynamic-range limited by artefacts around the bright core, with an off-source rms around 1.8 mJy beam^{-1}. Images presented in this paper are corrected for attenuation due to the primary beam of the VLA.

3 RESULTS

Fig. 1 shows a Gaussian-smoothed image of the X-ray emission surrounding the south-west radio lobe with radio contours overlaid. It can be seen that the shell is sharply edge-brightened. We interpret the outermost edge of the X-ray emission as the shock front. This lies ∼16 arcsec from the outer edge of the radio lobe, which is well defined in our radio images, as demonstrated by the radio and X-ray surface brightness profiles shown in Fig. 2, extracted for the regions shown in the bottom right-hand panel of Fig. 3. We interpret the sharp radio lobe boundary to be the contact discontinuity. Shell emission is seen throughout the lobe region, including a bright region on the northern edge of the shell, a distance of 1.4 arcmin E of the nucleus, which was first discussed by Kraft et al. (2007a). The fact that the X-ray emission clearly extends a significant distance beyond the edge of the radio lobe (well defined in our high resolution radio maps) and is edge-brightened (see Fig. 2) strongly supports a model in which the X-ray emission originates in a shell surrounding the radio lobes, rather than originating in a fluid contained within them.

We initially. carried out spectral analysis for several large regions to determine the global properties of the shell X-ray emission. The spectral extraction regions are shown in Fig. 3. Spectra were extracted from all seven data sets using the CIAO task *specextract*,

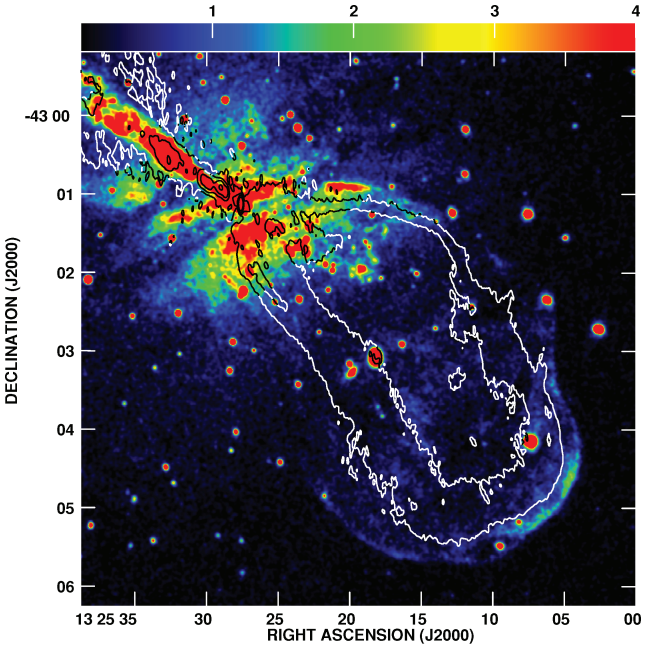

Figure 1. The shell of X-ray emission surrounding the SW lobe, from the merged *Chandra* data from all observations to date, in the 0.4–2.5 keV energy range. The image has been lightly smoothed with a Gaussian kernel of FWHM 2.3 arcsec. Radio contours at 1.4 GHz are overlaid with contour levels 9.0 × (1, 4, 16, 64) mJy beam^{-1}. The colour scale is linear in units of ACIS counts pixel^{-1}

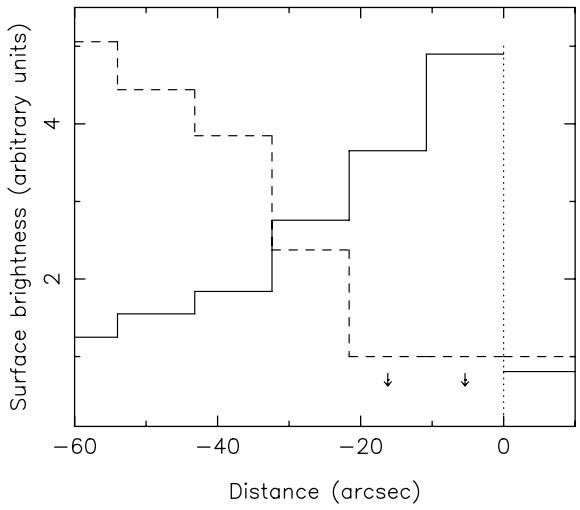

Figure 2. X-ray (solid line) and radio (dashed line) surface brightness profiles across the shock front (the extraction regions are shown in Fig. 3). Arrow symbols indicate positions at which the radio profile is based on (3σ) upper limits. The profiles have been renormalized for ease of comparison. The dotted line indicates the position of the shock front as determined from the X-ray data. The bin width is significantly larger than the size of the radio beam, so that all data points are independent.

which also calculates appropriate response files. The background regions used are also shown in Fig. 3. For the background spectra, additional exclusion regions were included on an observation-by-observation basis to mask any out-of-field-of-view regions and chip gaps. Point sources were also excluded from all of the extracted spectra. The spectra were fitted in the 0.4–3.0 keV energy range to minimize background contamination from the wings of the point spread function (PSF) from the very bright central active galactic nucleus (AGN; e.g. Evans et al. 2004), which dominate above 3.0 keV across the entire field of view (e.g. Kraft et al. 2007a). This choice of energy range also minimizes any contamination from readout streaks. In the few cases, where readout streaks pass through regions of interest (e.g. ObsID 7800 for Region 3, and ObsIDs 7797 and 8490 for a small number of inner regions discussed in Section 3.3), we checked that excluding the data sets that could be contaminated did not affect the spectral results. For each region, we carried out joint fits to the spectra from all epochs, and we assumed a fixed hydrogen column density at the Galactic value of $N_{\rm H} = 8.4 \times 10^{20}\,{\rm cm}^{-2}$ (Dickey & Lockman 1990), except where otherwise specified. This is reasonable in general, as our spectral extraction regions are mainly well away from the central region where varying absorption from gas associated with the dust lane needs to be taken into account. For each of the regions, we initially fitted five spectral models: an APEC (Astrophysical Plasma Emission Code; Smith et al. 2001) model with free abundance (Model I), an APEC model with abundance fixed at $0.15\,{\rm Z}_{\odot}$ (Model II), an APEC model with abundance fixed at $0.5\,{\rm Z}_{\odot}$ (Model III), a single power-law model (Model IV) and a model consisting of an APEC ($Z = 0.5$) plus a power-law component (Model V). The abundance values for Models II and III were chosen to sample the range of abundances from the low values found in free-abundance fits to more typical values for galaxy atmospheres (e.g. David el al. 2006). Complete results of all the spectral fits are given in Table 1. Quoted errors are 1σ for one or two interesting parameters except where otherwise specified.

3.1 The bright outer shell emission

We first considered a region encompassing all of the bright shell emission (Region 1 in Fig. 3), with point sources excluded. While the spectral model parameters vary somewhat across this large region, the general features of the model fits described below are present in all the fits from smaller regions when Region 1 is subdivided. For this region, we find that Models IV and V (single power law and 2-component power-law plus APEC, respectively) give the best fits to the spectra. Models I–III (thermal models) give much poorer fits. Model I, the free abundance fit, has the lowest χ^2 of all of the thermal models; however, the abundance is constrained to be extremely low (a 3σ upper limit on Z of $0.007\,{\rm Z}_{\odot}$), and the fitting statistic is still significantly poorer than for the power-law fit (Model IV). For Model V (APEC plus power law), the inclusion of a thermal component does not significantly improve the fit when compared to Model IV, and the thermal model contributes an unabsorbed 0.4–3.0 keV flux of $\sim 1.6 \times 10^{-14}\,{\rm erg\,cm^{-2}\,s^{-1}}$, whereas the power law contributes a flux of $\sim 4.7 \times 10^{-13}\,{\rm erg\,cm^{-2}\,s^{-1}}$, a factor of 30 times higher. The spectrum for Region 1 is shown in Fig. 4 with each of the five models overplotted. The fitting statistics for this region are fairly poor for all five models. This is likely to be due to radial variation in the spectral properties of the emission, possibly including variation in the contribution from thermal emission. We explore this spatial variation in Section 3.3.

To summarize, we find that a single power law is a better description of the spectrum than any thermal models. In addition, the fitted temperature values for thermal models are strongly dependent on the adopted abundance. The shallower observations analysed by Kraft et al. (2003, 2007a) meant that thermal models provided an adequate fit to the data, but with our deeper data, we are now able to rule out a simple, single-temperature APEC model at high confidence. In particular, the thermal fits have large residuals at soft energies. Fitting a two-temperature APEC model

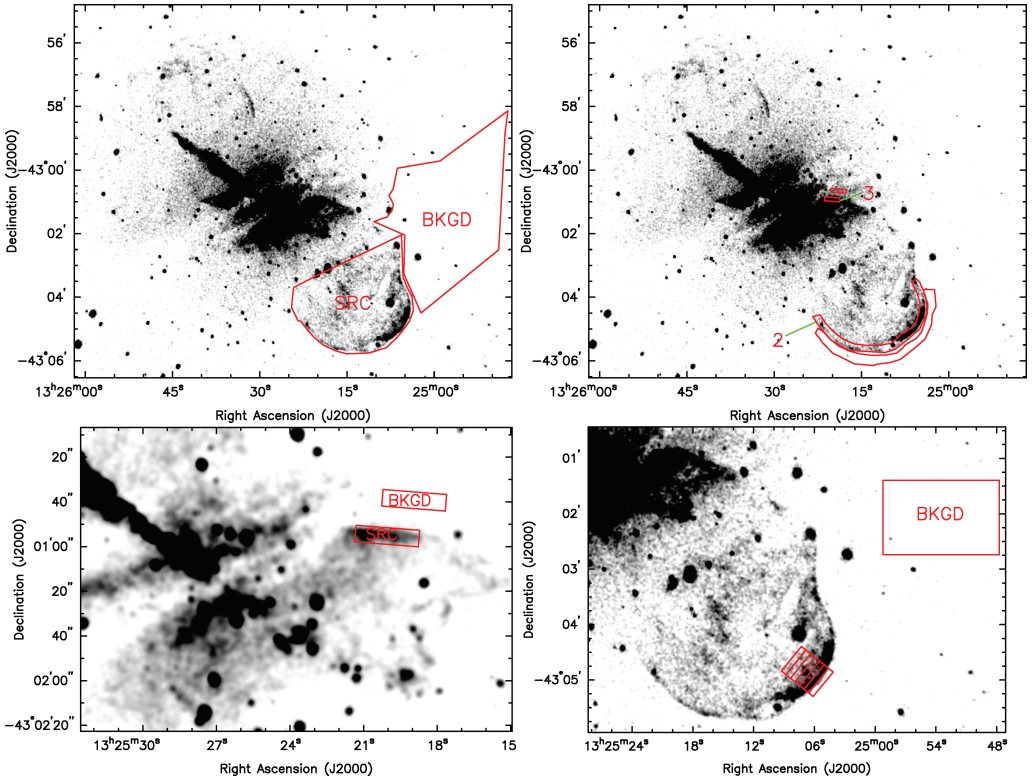

Figure 3. Source and background regions used for the spectral and spatial analysis. Top left: Region 1, which includes the brightest part of the shell emission; top right: Regions 2 and 3, the region of X-ray shell emission exterior to the radio lobe (bottom right of the image) and the region of bright emission at the north-east edge of the lobe, respectively; bottom left: zoomed-in view of Region 3, the north-east edge of the SW shell; bottom right: regions used for surface brightness profile in Fig. 2. Chip gaps and out of field-of-view regions were masked out of background spectra on an observation by observation basis as necessary, and point sources were excluded from all spectra.

Table 1. Model fits to X-ray spectra. All fits are joint fits to spectra from all seven observations in the energy band 0.4–3.0 keV. Galactic absorption of 8.4×10^{20} cm^{-2} was assumed for all of the fits. For Model V, we list the inferred, unabsorbed 0.4–3.0 keV fluxes for each model component as a measure of the relative importance of thermal and non-thermal emission in each region.

Model		Parameter	Region 1	Region 2	Region 3
Model I:	*APEC* (free abundance)	kT (keV)	$1.60^{+0.07}_{-0.06}$	$2.03^{+0.24}_{-0.14}$	$0.91^{+0.04}_{-0.04}$
		Z ($Z_\odot$)	< 0.007	< 0.05	$0.17^{+0.05}_{-0.04}$
		χ^2 (d.o.f.)	1010 (743)	344 (308)	137 (97)
Model II:	*APEC* (fixed abundance)	kT (keV)	$2.22^{+0.08}_{-0.06}$	$2.59^{+0.13}_{-0.13}$	$0.90^{+0.03}_{-0.02}$
		Z ($Z_\odot$)	0.15	0.15	0.15
		χ^2 (d.o.f.)	1213 (744)	377 (309)	138 (98)
Model III:	*APEC* (fixed abundance)	kT (keV)	$3.26^{+0.09}_{-0.09}$	$3.58^{+0.24}_{-0.19}$	$0.97^{+0.01}_{-0.02}$
		Z ($Z_\odot$)	0.5	0.5	0.5
		χ^2 (d.o.f.)	1478 (744)	437 (309)	177 (98)
Model IV:	power law	Γ	$2.20^{+0.02}_{-0.02}$	$2.01^{+0.04}_{-0.03}$	$2.54^{+0.05}_{-0.05}$
		χ^2 (d.o.f.)	931 (744)	333 (309)	445 (98)
Model V:	*APEC* + *power law*	kT (keV)	$0.23^{+0.09}_{-0.08}$	0.93[a]	$0.89^{+0.05}_{-0.06}$
		Z ($Z_\odot$)	0.5	0.5	0.5
		Γ	$2.15^{+0.06}_{-0.05}$	$2.00^{+0.15}_{-0.06}$	$2.13^{+0.30}_{-0.27}$
		χ^2 (d.o.f.)	928 (742)	332 (307)	141 (96)
		$F_{\rm apec}$	$(1.4^{+0.8}_{-1.2}) \times 10^{-14}$	$<4.8 \times 10^{-14}$	$(2.0 \pm 0.2) \times 10^{-14}$
		$F_{\rm PL}$	$(4.7^{+0.1}_{-0.2}) \times 10^{-13}$	$(1.38^{+0.05}_{-0.07}) \times 10^{-13}$	$(9.2^{+2.7}_{-2.6}) \times 10^{-15}$

[a]The temperature was completely unconstrained for this model.

can mitigate this problem to some extent: we find best-fitting temperatures of 0.28 ± 0.02 and 3.90 ± 0.26 keV, assuming 0.5 times solar abundances. This fit has χ^2 of 1065 for 742 d.o.f., which is a significant improvement on the single temperature models for realistic abundances, but still considerably poorer than the power-law fit.

In order to firmly rule out a thermal origin for the shell emission, we also considered the limits on the 6.7 keV line from

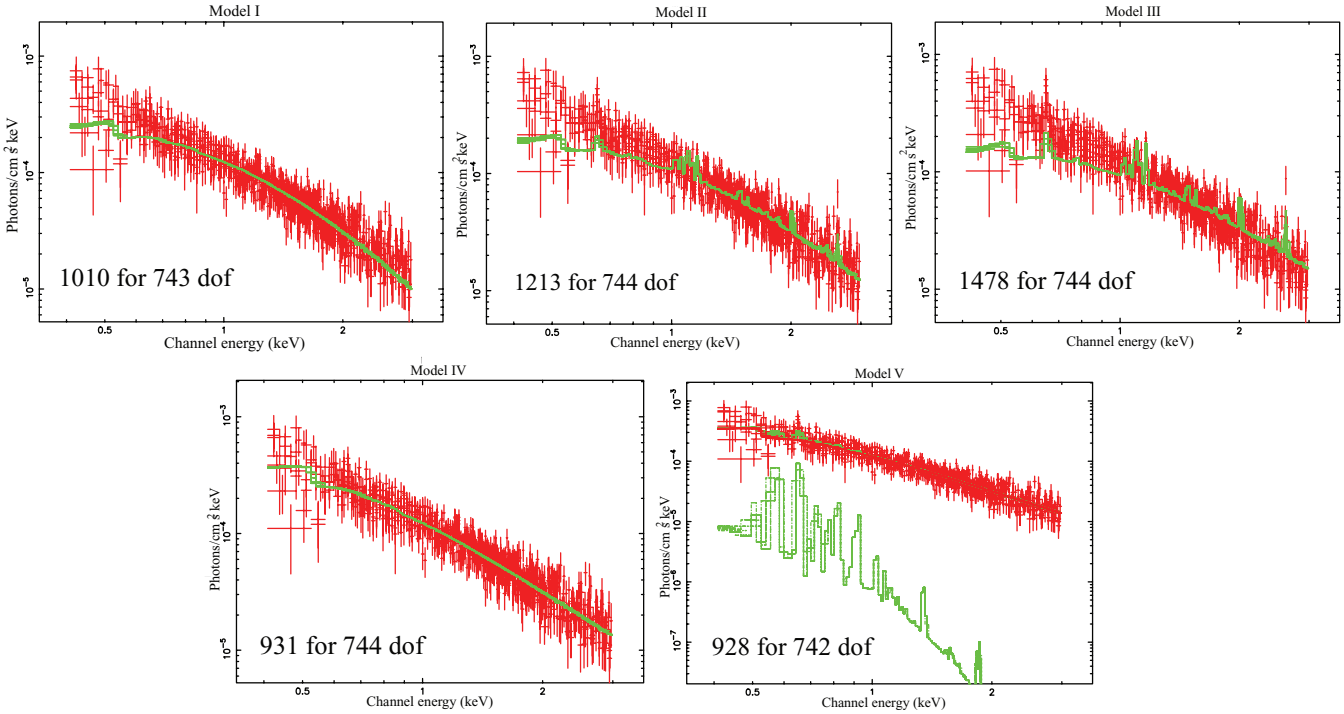

Figure 4. Spectral fits for Region 1. Top left: Model I (free-abundance APEC), middle: Model II (APEC with $Z = 0.15\,Z_{\odot}$), right-hand side: Model III (APEC with $Z = 0.5\,Z_{\odot}$), bottom left: Model IV (power law), right-hand side: Model V (power law + fixed-abundance APEC). The data are in red and the fitted models are in green. The *y*-axis scale is different for Model V due to the inclusion of the thermal component, which has a low flux.

ionized Fe, and the Fe L complex, for assumed gas temperatures of 1.5 and 3 keV (spanning the range seen in the thermal spectral fits). We found that the limits on the 6.7 keV line do not provide strong constraints, but the predicted fluxes in the Fe L complex at 1.17 keV for an abundance of $0.15\,Z_{\odot}$ are 1.6×10^{-5} and 4×10^{-6} photons cm^{-2} s^{-1}, respectively, whereas the 3σ upper limit from our joint fits (using the linewidth and energy of a broad Gaussian fit to the complex in a faked spectrum of the same parameters) is $\sim 2 \times 10^{-6}$ photons cm^{-2} s^{-1}. Hence, there is no evidence for the line emission expected from a thermal plasma with realistic temperature and abundance values. We cannot rule out a model in which turbulent broadening has erased the lines from the spectrum, but this would require turbulent velocities at or well above the sound speed of the gas.

We also examined separately the brightest region of shell emission at the south-west rim, ∼5.6 arcmin to the south-west (SW) of the nucleus (Region 2 in Fig. 3), which is external to the radio lobes (see Fig. 2), to construct a broad-band spectral energy distribution for the shell without contamination from any possible radio lobe emission (see below). Details of the spectral fits are in Table 1. The overall conclusions of the spectral analysis for this region are very similar to those for Region 1; this is, the spectrum is much better fitted by a non-thermal power-law component rather than thermal emission. This is as expected given that this region contributes a significant fraction of the flux in Region 1.

We therefore conclude that the shell emission is likely to be non-thermal, in contrast to the conclusions of earlier work based on poorer quality spectra.

3.2 The north-east edge of the shell

As shown in Fig. 1, there is a small region of brighter shell emission at the northern edge of the SW shell close the AGN (∼1.4 arcmin east of the nucleus: Region 3 in Fig. 3). This region was shown to be associated with the shell and examined in detail by Kraft et al. (2007a), who concluded that the emission was thermal, and significantly cooler than at the outer, SW edge of the shell (0.6–0.8 keV for their S1 and S2 regions for an assumed abundance of $0.5\,Z_{\odot}$). Since the line emission is expected to be stronger at these temperatures, this region can potentially provide useful constraints on the shell X-ray emission. We therefore examined spectra for Region 3 (Fig. 3), which is similar to Kraft et al. (2007a)'s S1 region. Results are listed in Table 1.

In contrast to the situation in Region 1 and subregions of the outer shell, we find that a thermal model is strongly favoured in this region. With a free abundance fit, we obtain a best-fitting temperature of 0.91 ± 0.04 keV and an abundance of $0.17^{+0.05}_{-0.04}\,Z_{\odot}$ with $\chi^2 = 137$ for 97 d.o.f. The Fe L complex is very prominent in the spectrum, which cannot be fitted adequately with a power-law model. The inclusion of a power-law component to the model, in addition to the APEC, does not improve the fit. Hence, we conclude that the X-ray emission from this region is unambiguously thermal. The best-fitting abundance is significantly lower than that expected from the galaxy ISM, which is likely to be due to the assumption of a single temperature (e.g. Buote 2000). As our spectral regions are likely to include multitemperature gas, we cannot obtain a reliable estimate of the metallicity from the X-ray data. We therefore chose to adopt a metallicity of $Z = 0.5\,Z_{\odot}$, more appropriate for a galaxy halo. The single temperature fits also showed strong residuals at ∼1.35 keV, likely to be due to Mg XI, and so we chose to include a narrow Gaussian at this energy. The best-fitting temperature for an APEC model with fixed abundance plus 1.35 keV Gaussian is $0.95^{+0.03}_{-0.02}$ keV, with $\chi^2 = 145$ for 97 d.o.f. We also investigated whether additional Silicon features are present in the spectrum as would be expected if the gas is overabundant in alpha elements. We found a significant improvement in the fit if a Gaussian is added at

1.865 keV, corresponding to Si XIII, and a marginal improvement including a Gaussian at 2.006 keV, corresponding to Si XIV. Using the varial abundance APEC (VAPEC) model with all other elements fixed at an abundance of 0.5 times solar (which gives a very similar fit), we find a magnesium abundance of $2.4^{+0.3}_{-0.4}$ times solar. If the silicon abundance is allowed to vary, an abundance of $1.2^{+0.3}_{-0.2}$ times solar is obtained. The data are therefore consistent with a model in which the shocked gas in this region is alpha enriched. It is also possible that the unexpectedly strong magnesium and silicon lines are indicative of a non-equilibrium ionization state. We note that there is also some evidence of enhanced magnesium and silicon abundance in the ISM exterior to Region 3 (Kraft et al., in preparation).

As Region 3 is comparatively close to the nucleus, we investigated whether additional absorption, for example, from the dust lane, was present. We found that allowing the absorbing column to vary caused an increase in $N_{\rm H}$ of a factor of $\sim$2, with a small improvement in the fitting statistic; however, the best-fitting temperatures and normalizations were not significantly affected, and so we adopt the fits with Galactic absorption discussed above.

It is likely that there is complicated temperature structure in the shell that we cannot resolve, and as the gas in this region is assumed to have passed through the shock front recently, it is likely that the ionization balance has been affected by the shock. We fitted non-equilibrium ionization models to the spectra for Region 3 (the *nei* model in XSPEC), and found a fit of similar quality to that for the APEC model with a Gaussian at 1.35 keV, with a very similar temperature and normalization to our adopted model. Our conclusions should not be strongly affected if the gas is far from ionization equilibrium. It is likely that our spectral extraction region contains gas with a range of temperatures and ionization states; however, any effect this has on our conclusions below about the gas density and shock dynamics is likely to be smaller than the uncertainties introduced by our geometric assumptions in Section 4.2. In addition, the electron and proton fluids in the shocked plasma may not be in equilibrium (e.g. Kraft et al. 2007a). We discuss this possibility further in Section 4.3.

As we are unable to constrain these effects with our data, we adopt the simple, fixed abundance, single-temperature model with Gaussian component to account for the prominent Mg line, as discussed above. We adopt an abundance of $Z = 0.5$ times solar to compute gas density and pressure, rather than the lower value from the free abundance fit, as this is likely to be artificially low due to using a single temperature model, as discussed above. As the X-ray emissivity is due to both continuum mainly from hydrogen and helium and line emission from heavy elements and varies with the square of density, the inferred gas density varies at most as $Z^{1/2}$. Thus, the assumed abundance will introduce uncertainties of the order of 10 per cent at most.

3.3 Spectral structure of the shell

We divided the entire lobe into small regions to map the spectral structure across the shell. The regions were defined by requiring a minimum of 2000 0.4–2.5 keV counts (before background subtraction) to allow good constraints to be obtained on the spectral parameters. Background spectra were extracted from a region adjacent to the shell at the same radius as the source region, in order to subtract correctly the emission from the galaxy ISM and from the wings of the nuclear PSF. This resulted in a total of 50 regions, each of which was fitted separately with APEC (Model III) and power-law (Model IV) models in the same way as for the fits for larger regions described above. Fig. 5 shows a spectral index map for the power-law fits (top panel), and a temperature map obtained using the APEC fits (middle panel). For each spectral map, a corresponding map of the fit statistic (χ^2/n) is also shown.

As expected from our analysis above, the inner regions of the shell (close to the AGN) have very different spectral properties to those in the outer parts (e.g. Region 1) – for the power-law fits, the inner parts have much steeper spectral indices (and often very poor fit statistics), consistent with a thermal interpretation for these regions. In the region between $\sim$2 and $\sim$3 arcmin from the nucleus none of the fits is good. This is partly because the emission there has lower surface brightness than elsewhere, but mainly due to contamination from the wings of the PSF from the bright transient source at this radius (Sivakoff et al. 2008). The outer parts are best fitted by a power law, with the spectral index varying from $\sim$1.7 to $\sim$2.4, consistent with a predominantly synchrotron origin.

The bottom left-hand panel of Fig. 5 shows a plot of spectral index as a function of distance from the central AGN. For this analysis, we defined a set of annuli centred on the nucleus, and extracted spectra from regions consisting of the intersection of each annulus with a polygon enclosing the shell region. We find that the spectral index is steepest in the central regions, where the power-law fit is not a good representation of the data. In the outer regions, the spectral index remains fairly close to a value of 2, but there is a statistically significant decline in the spectral index in the last three bins. This trend is present whether the results of Model IV or V are adopted. This is discussed further in Section 4.2.

We also investigated the contributions of thermal and non-thermal emission to the observed flux as a function of distance from the nucleus by fitting Model V (APEC + power law) to the same regions as for the spectral index plot discussed in the previous paragraph. The bottom right-hand panel of Fig. 5 shows the fraction of the total unabsorbed 0.4–3.0 keV flux in the thermal and non-thermal model components as a function of distance from the nucleus, indicating that the X-ray flux is dominated by non-thermal emission except in the very inner regions. The strong evidence for dominance by thermal emission in Region 2 leads us to conclude that this is likely to be a real difference in the shell emission, rather than an artefact of poor background subtraction.

4 DISCUSSION

Our spectral analysis of the X-ray shell emission strongly favours a non-thermal interpretation for the majority of the X-ray emission in the outer half of the shell, due to the unrealistically low abundances required by thermal models, as well as the lack of expected emission-line signatures, particularly the Fe L shell complex. These results, together with the strong resemblance between the highly edge-brightened shell emission and the X-ray emission from synchrotron-dominated supernova remnants (SNRs), such as SN1006 (e.g. Rothenflug et al. 2004), lead us to conclude that an X-ray synchrotron origin for the majority of the X-ray shell emission from Cen A is viable. Further constraints on this model come from limits at other wavelengths. It might be expected that a plausible energy distribution for an electron population producing X-ray synchrotron emission would also produce detectable emission at radio, optical, ultraviolet (UV) or infrared (IR) wavelengths, and so the model must pass this test. It must also be possible to construct a self-consistent picture of the radio-lobe dynamics, which explains both the strong thermal emission from Region 3 and the lack of any thermal signatures in the outer rim region. Below we discuss the constraints on a synchrotron model that can be obtained from multiwavelength measurements and from an analysis of the shock

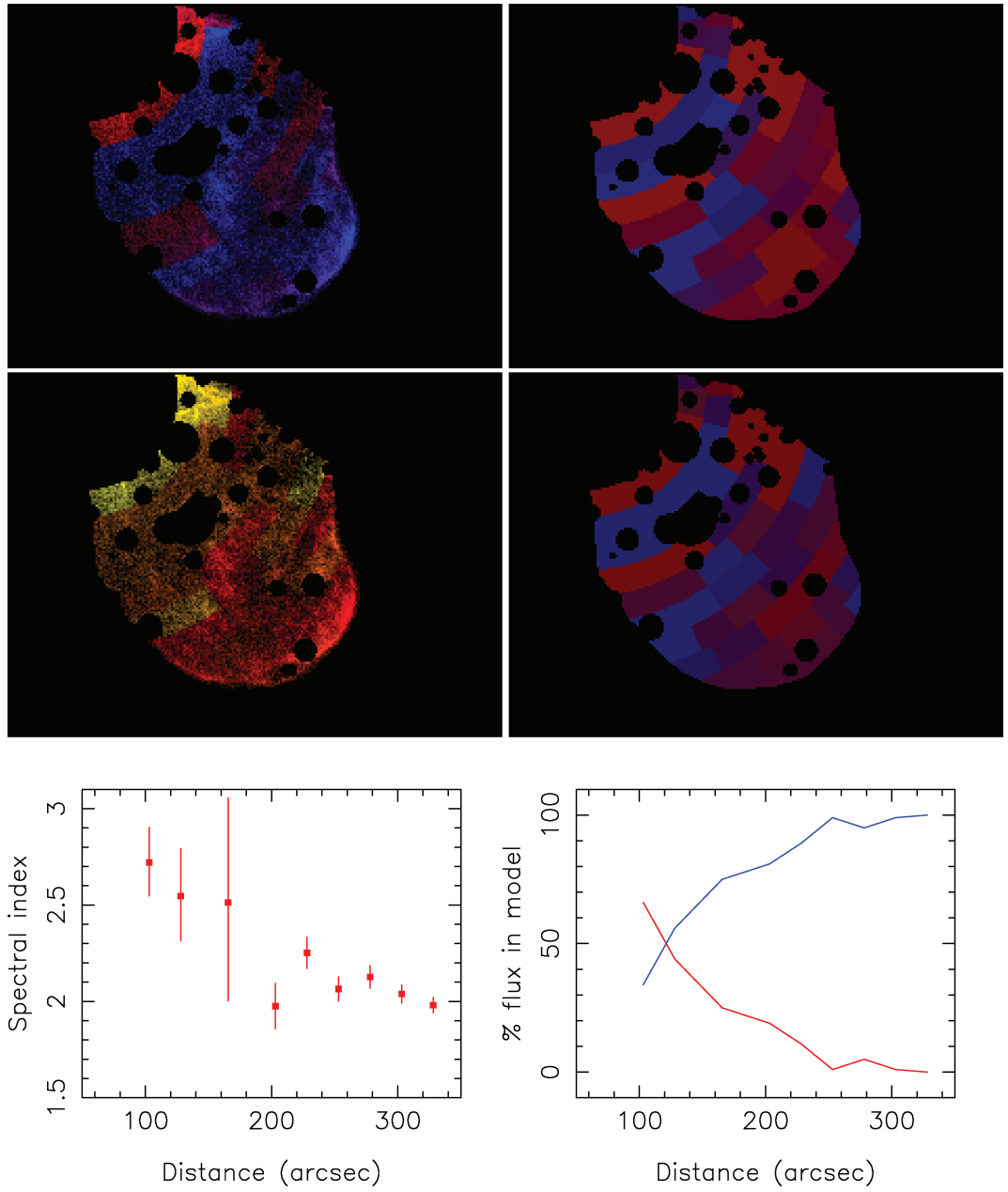

Figure 5. Spectral structure across the shell, as discussed in Section 3.3. Top: spectral index map, assuming Model IV (power law) for all regions (left-hand side: blue = 1.5, red = 4.0), with corresponding map of χ^2/n (right-hand side: red = 0.5, blue = 2.5). Middle: temperature map, assuming Model III (APEC with $Z = 0.5$) for all regions (left-hand side: red = 4.0 keV, yellow = 0.7 keV), with corresponding map of χ^2/n (right-hand side: red = 0.5, blue = 2.5). Bottom left: spectral index as a function of distance from the nucleus. The large error bar for the third data point is because a large fraction of this region is excluded due to a bright X-ray transient present in several data sets (Sivakoff et al. 2008). Bottom right: fraction of flux in thermal (red) and non-thermal (blue) components for Model V as a function of distance from the nucleus.

conditions and lobe dynamics. We also consider the dependence of our conclusions on the assumption of electron-ion equilibrium. Finally, we consider the implications of our results for particle acceleration in Cen A and other radio galaxies, and for Cen A as a source of ultra-high energy cosmic rays (UHECRs) and TeV emission.

4.1 The broad-band SED of the shell region

The brightest part of the X-ray shell surrounding Cen A's SW lobe is the outer rim, which is spatially separated from the region coincident with the radio emission from the radio lobe itself. If the X-ray emission from the shell is produced via the synchrotron process, then it would be expected to originate in an electron population that extends to energies much lower than those emitting in the X-ray band. No shell emission has been reported previously at radio, optical, IR, UV or radio wavelengths. We determined limits in the radio, IR and UV using VLA, *Spitzer* and the *Galaxy Evolution Explorer* (*GALEX*) observations to construct a broad-band SED (Fig. 6) for a region of shell emission surrounding the radio lobe (we used Region 2, discussed above, which is exterior to the radio lobe in projection, so as to obtain as tight a radio constraint as possible).

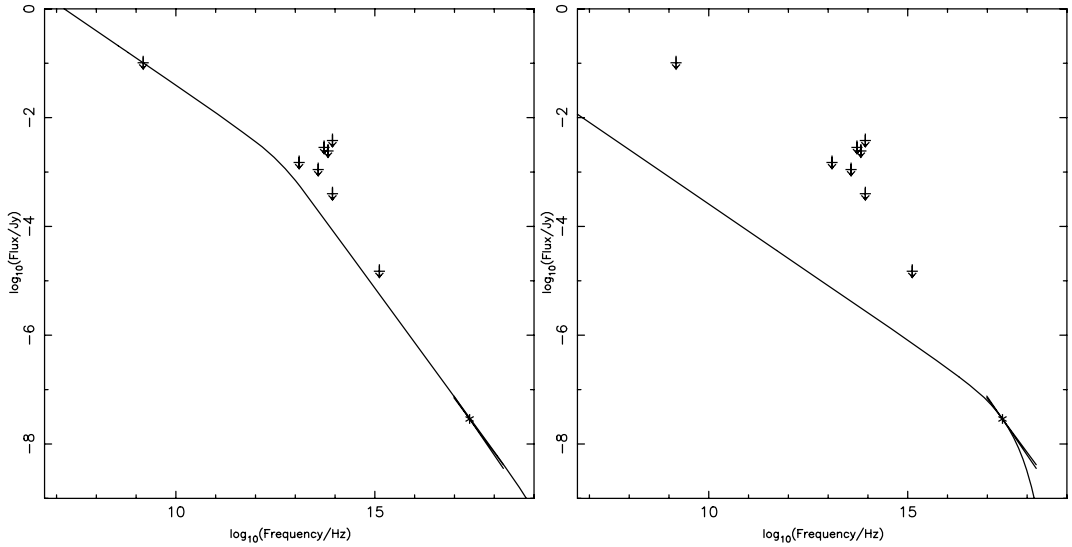

Figure 6. The broad-band SED for Region 2, including upper limits at 1.4-GHz, 3.6, 4.5, 5.8, 8.0 and 24 μm, 231 nm, and the measured X-ray flux density at 1 keV and spectral index. Solid line is a synchrotron model fit with (l) $\alpha = 0.5$, $\gamma_{\rm min} = 10$, $\gamma_{\rm break} = 4.4 \times 10^4$, $\gamma_{\rm max} = 5 \times 10^9$ (discussed in Section 4.1), and (right-hand panel) $\alpha = 0.5$, no break, and $\gamma_{\rm max} = 3 \times 10^8$ (discussed in Section 4.4).

The radio limit shown in Fig. 6 was obtained from the 1.5-GHz radio map described in Section 2 and is a 3σ limit based on the off-source rms noise, as there is no detection of radio emission from Region 2. We used the *Spitzer* Infrared Array Camera (IRAC) and Multiband Imaging Photometer (MIPS) (Brookes et al. 2006; Hardcastle, Kraft & Worrall 2006) and GALEX observations (Neff, Schiminovich & Martin 2003; Hardcastle, Kraft & Worrall 2006) to obtain IR limits at 3.6, 4.5, 5.8, 8.0 and 24 μm and a UV limit at 231 nm. The analysis was carried out as described in Hardcastle et al. (2006). Limits were calculated for Region 2, using a larger region immediately outside Region 2 as a background. At all bands from the IR to the UV, the dominant background is stars, and so this choice of background will give a strict upper limit. As an alternative strategy, we also used galaxy-subtracted IR images to obtain tighter limits on the IR emission from the shell. This allowed us to decrease the upper limit at 3.6 μm by roughly an order of magnitude. Similar improvements could be obtained using this method at other wavelengths, but would not significantly affect the constraints on a synchrotron model, as discussed below. Fig. 6 includes all of the limits obtained, including the galaxy-subtracted limit at 3.6 μm.

Fig. 6 shows a synchrotron model chosen to fit through both the X-ray data point and spectral index and the 1.4-GHz upper limit. The plotted model assumes $\alpha = 0.5, \gamma_{\rm min} = 10$, $\gamma_{\rm break} = 4.4 \times 10^4, \gamma_{\rm max} = 5 \times 10^9$, and uses the 1.4-GHz upper limit to normalise the electron spectrum, assuming equipartition in the shell material. The volume enclosed in Region 2 was modelled by approximating to a box of dimensions $573 \times 7 \times 46$ arcsec^3, where the length and width are the dimensions of the extraction region, and the depth is approximated by that halfway between the inner and outer curved boundaries of the regions, assuming a spherical shell of appropriate radius to fit the shell curvature. This gives a volume of $\sim 3 \times 10^{64}$ cm^3. None of the IR or UV limits can rule out the synchrotron model described above. In addition, since the radio data point is an upper limit, a model with a significantly higher break frequency (as typically found for SNRs with X-ray synchrotron emission, e.g. Rho et al. 2003; Dyer, Reynolds & Borkowski 2004; see also Section 4.4), which could be orders of magnitude below the IR limits, also cannot be ruled out (see the right hand panel of Fig. 6). Hence, we conclude that the broadband SED for the rim of the Cen A SW shell is consistent with a synchrotron interpretation for the X-ray emission.

Although a non-thermal contribution to the spectrum in the NE part of the shell (Region 3) is not required, the limits on a power-law contribution to the Region 3 spectrum from fitting Model V are consistent with a significant flux from synchrotron emission in this region (the fit for Model V implies an unabsorbed 1-keV flux density from the power-law component of ∼2 nJy). Therefore, we cannot rule out significant particle acceleration in Region 3 as well.

Finally, we also investigated whether inverse Compton emission could explain some or all of the shell X-ray emission. X-ray emission from inverse-Compton (IC) scatting could be significant in the regions coincident with the radio lobes (whose X-ray emission we have hitherto been interpreting as coming from the shell material in front of and behind the lobe). We therefore modelled the electron distribution in the radio lobe in order to predict the expected level of IC emission. We approximated the lobe as a cylinder of length 270 arcsec and radius 80 arcsec, using radio flux measurements at 240 MHz and 8 GHz to determine the shape and normalization of the electron distribution, assuming equipartition. We assumed $\gamma_{\rm min} = 10$, as above, and chose $\gamma_{\rm max}$ to fit the observed radio spectrum, giving a value of 1.2×10^4. The predicted 1-keV flux density for the lobe from IC scattering of the cosmic microwave background (CMB) radiation (the dominant process) and synchrotron self-Compton (SSC) is ∼3.3 nJy, which is a factor of ∼30 below the observed flux from the lobe region. Hence, it is possible that a small fraction of the observed X-ray flux from Region 1 is produced by the IC/CMB process. For the lobe emission to be produced entirely by IC/CMB would require a magnetic field a factor of ∼6 below equipartition. An IC model for the edge-brightened rim of the X-ray structure (e.g. Region 2) is implausible, due to our tight limits on the radio emission in this region, and because none of the many examples of IC/CMB-detected lobes (e.g. Croston et al. 2005) shows edge brightening. We therefore consider it unlikely that our conclusions are affected by possible contamination from X-ray IC emission.

4.2 Lobe expansion and shock dynamics in a synchrotron model

As the X-ray emission from the north-east region of the shell (Region 3) is unambiguously thermal in origin (see Section 3.2), this is the best region to use for investigating the shock jump conditions. We approximated the volume of shell enclosed within Region 3 as a box of dimensions $0.480 \times 0.127 \times 0.769$ arcmin^3, where the length and width are the dimensions of the spectral extraction region, and the depth along the line of sight was taken to be the chord of a circle having the curvature of the outer edge of the shell in the north-east region at a distance halfway between the inner and outer edges of the spectral extraction region. This leads to an assumed volume of 1.7×10^{63} cm^3. With this volume, and assuming the APEC + Gaussian model described in Section 3.2, we obtain a density of $n_{\rm p} = 0.033\,{\rm cm}^{-3}$, which corresponds to a pressure in the shocked gas of 1.1×10^{-10} dyne cm^{-2}, assuming $kT = 0.95$ keV as discussed above. The shell density in Region 3 is roughly 3.5 times the density of the ISM at this distance, based on the beta model fitted to the external gas density distribution by Kraft et al. (2003). The deeper *Chandra* data give a consistent value for the density at this radius; however, we note that the ISM density is not well constrained because the distribution of gas is likely to deviate significantly from spherical symmetry, and to be inhomogeneous in the inner regions of the galaxy. Hence, the density contrast is consistent with the value of 4 expected for a strong shock, as was concluded previously by Kraft et al. (2007a). If the hot-gas shell and radio lobe are assumed to be in pressure balance, then the pressure inside the radio lobe is expected to be $\sim 1.1 \times 10^{-10}$ dyne cm^{-2}, as calculated above, which is about an order of magnitude higher than the lobe minimum pressure. This is of the same order as the differences between lobe minimum pressures and external pressures for Fanaro–Riley type I (FR I) radio galaxies in general (e.g. Croston et al. 2007; Croston et al. 2008). The pressure contrast between the shell and the ISM is $P_{\rm shell}/P_{\rm ism} = 10$, using the external gas density distribution and temperature from Kraft et al. (2003). We note that the temperature of the ISM is poorly constrained due to spatially varying absorption and abundance uncertainties. Assuming ram-pressure balance and that $\gamma = 5/3$, this estimated pressure jump implies that, at its north-east edge, the radio lobe is expanding at a Mach number of $\sim$2.8, which corresponds to an expansion speed of $\sim 850\,{\rm km\,s}^{-1}$.

Kraft et al. (2003) found that the apparent density contrast between shocked and unshocked gas in the outer parts of the shell (assuming a thermal interpretation for all the shell X-ray emission) is much higher than the prediction for a strong shock, and derived the expansion speed assuming that the observed shell is shocked gas that has cooled rather than the component that directly enters the jump equations for shocked gas. A non-thermal model for most of the X-ray emission within the shell can provide a simpler interpretation of the larger X-ray-intensity contrast inside and outside the shell. We checked the low apparent contribution from thermal emission in the outer regions of the shell is consistent with the thermal emission expected from a shell of shocked gas a factor of 4 denser than the ISM in the shell's outer regions (for several assumed temperatures). We assumed an unshocked ISM density of 1.0×10^{-3} cm^{-3} at the outer edge of the shell [Kraft et al., in preparation; note that this is a factor of 1.7 lower than that assumed by Kraft et al. (2003) and Kraft et al. (2007b)], so that the shell gas would be expected to have a density of $\sim 4 \times 10^{-3}$ cm^{-3}. We calculated the volume corresponding to the outer shell region discussed in Section 3.1 assuming a half spherical shell of outer radius 121 arcsec. We estimated the thickness of the shell using the 1.4-GHz radio map and the merged 0.4–2.5 keV event file by measuring the separation between the edge of the radio lobe and the brightest part of the shell edge. We took the average of three measurements around the edge of the shell, giving a mean thickness of 16.3 ± 1.5 arcsec, where the measurement uncertainty (which may be partly due to real variations in the thickness of the shock front) is larger than any astrometric uncertainty or resolution effects. Our measured shell thickness is consistent with the value of 17 arcsec adopted by Kraft et al. (2007a). This assumed geometry leads to an expected emission measure of $\sim 1.7 \times 10^{58}$ cm^{-3} (corresponding to a 0.4–3.0 keV flux of 1.3×10^{-14} erg cm^{-2} s^{-1}). The measured normalization for the APEC component of Model V discussed in Section 3.1 corresponds to an emission measure more than 30 times higher, hence the data are consistent with this emission being present. However, as the APEC component in the spectrum of this region is not required by the data, the spectra can also be well fitted by an APEC + power-law model with the APEC normalization fixed at the value corresponding to the expected emission measure, for any reasonable temperature (e.g. between $kT = 0.5$ and 15.0 keV – our adopted shock model as discussed below implies a post-shock temperature of $\sim$11 keV). In all cases, the thermal contribution to the fit is negligible. Hence, the X-ray spectra for the outer shell are consistent with a model in which a strong shock is occurring, with the X-ray emission dominated by synchrotron emission from high-energy particle acceleration.

If we assume that the radio lobe is isobaric, and that the radio lobe and shocked gas are in pressure balance everywhere, then the pressure in the shocked gas shell at its outer edge (e.g. Region 2) should be the same as the lobe internal pressure and shell pressure in Region 3, which we calculated above. This implies that the expansion speed at the outer edge of the lobe where we see the brightest non-thermal emission should be much higher, given the significantly lower external gas density ($\sim 10^{-3}$ cm^{-3}). Assuming an ISM gas temperature of 0.35 keV (Kraft et al., in preparation), we obtain a pressure jump $P_{\rm shell}/P_{\rm ism} \sim 87$, corresponding to a Mach number of $\sim$8.4, and a lobe expansion speed at its outer edge of $\sim 2600\,{\rm km\,s}^{-1}$. This speed is similar to that inferred by Kraft et al. (2003). We can also infer a transverse expansion speed for the radio lobe similarly, using the external density at the lobe midpoint given by the profile in Kraft et al. (2003), which we find to be $\sim 1400\,{\rm km\,s}^{-1}$. The observed axial ratio of the radio lobe is roughly consistent with the inferred longitudinal and transverse expansion speeds for the lobe if the expansion has been self-similar throughout the source's lifetime (though in practice this is unlikely to have been the case). The adopted physical parameters for Regions 2 and 3 are summarized in Table 2.

As for Region 3, we have assumed here that $\gamma = 5/3$. This will be correct if the shell pressure is dominated by the thermal component

Table 2. Adopted physical parameters for Regions 2 and 3.

Parameter	Region 2	Region 3
$T_{\rm shell}$ (keV)	11.0	0.95
$T_{\rm ism}$ (keV)	0.35	0.35
Z ($Z_\odot$)	0.5	0.5
$n_{\rm p,shell}$ (cm^{-3})	0.004	0.033
$n_{\rm p,ism}$ (cm^{-3})	0.001	0.01
$P_{\rm shell}$ (dyne cm^{-2})	1.1×10^{-10}	1.1×10^{-10}
$P_{\rm ism}$ (dyne cm^{-2})	1.3×10^{-12}	1.1×10^{-11}

of the shocked gas, rather than by the pressure in the relativistic particles that are producing the observed X-ray synchrotron emission. As we concluded above, the observations are consistent with a scenario in which the hot shocked gas has the density expected for a strong shock, but is not separable from the dominant emission attributed to synchrotron radiation. However, we also checked whether the internal pressure of the synchrotron-emitting particles is likely to significantly alter the shock dynamics. Assuming the SED discussed in Section 4.1 with an equipartition magnetic field of $\sim$8 μG and no energetically significant protons, we find that the pressure in cosmic rays and magnetic field is $\sim 2 \times 10^{-12}$ dyne cm^{-2}, which is insignificant compared to the thermal pressure. We note that this is an upper limit on the pressure in the relativistic particles if in equipartition because the SED model is based on upper limits at radio, IR and UV wavelengths. Magnetic field strengths of $\sim$90 μG or higher, more than an order of magnitude higher than the equipartition value, would be required for the non-thermal (magnetic) pressure to dominate, assuming $\gamma_{\rm min} = 10$. A departure from equipartition in the direction of electron dominance could also lead to non-thermal pressure dominating over thermal pressure; however, this would also have to be extreme.

We can also estimate the total energy of the radio source and the power of the jet. Approximating the shock front as a prolate spheroid with semi-major axis 167.2 arcsec and semi-minor axis 115.0 arcsec, we find an enclosed volume of 1.6×10^{66} cm^3. The cavity enthalpy, $4PV$ is then 7×10^{56} erg. We make a rough estimate of the kinetic energy of the shell using the expansion speed midway along the shell, and the gas density for Region 1, to obtain $E_K = 1.2 \times 10^{56}$ erg. Assuming a constant expansion speed, we obtain a source age estimate of $\sim 2 \times 10^6$ yr, and hence we estimate a mean jet power over the source lifetime of $\sim 10^{43}$ erg s^{-1}. We can also estimate an instantaneous jet power as $P\dot{V}$, where $\dot{V} = V(\dot{a}/a + 2\dot{b}/b)$, with a and b the semimajor and semiminor axes, respectively. If the lobe expansion is self-similar, then $\dot{V} = 3V\dot{a}/a = 4\pi b^2 \dot{a}$. As one end of the expanding lobe is tied to the AGN, $2\dot{a} = v_{\rm shock}$, the shock expansion speed at its outer edge, and hence the instantaneous jet power, p, is given by $p = 2\pi P b^2 v_{\rm shock} = 6.6 \times 10^{42}$ erg s^{-1} (using the shock speed of 2600 km s^{-1} at the outer edge of the shock). This is roughly a factor of 15 times higher than the current radiative power of the AGN (Evans et al. 2004).

4.3 Electron-ion equilibrium in the shocked gas

Our conclusions about the shock dynamics in Section 4.2 depend strongly on our adopted spectral model for the thermal emission in Region 3. As discussed in Section 3.2, the region shows a somewhat unusual spectrum, with a prominent magnesium line, that is not well fitted by a single APEC model. As the gas in this region is assumed to have passed through the shock front recently, it is likely that the ionization balance has been affected by the shock, as discussed in Section 3.2. It is also likely that our spectral extraction region contains gas with a range of temperatures and ionization states, but in Section 3.2 we concluded that any effect on our conclusions about the gas density and shock dynamics is likely to be smaller than the uncertainties introduced by our geometric assumptions in Section 4.2. However, an additional complication is that the electron and ion fluids may not have achieved equilibrium, as was discussed in the context of earlier work on the Cen A shock by Kraft et al. (2007a).

For gas temperatures of $\sim$1 keV and below, and photon energies below $\sim$1 keV, at the energy resolution of ACIS-I the thermal continuum is submerged by lines, particularly those of the Fe L complex. This makes fitted temperatures insensitive to the continuum. If the gas is not in ionization equilibrium, the relationship between line strengths and gas temperature is model dependent, so that a detailed model of the shock and subsequent return to ionization equilibrium is required to determine the gas temperature accurately. On the other hand, the shape of the continuum is determined largely by the electron temperature. In the absence of a detailed model for the ionization state of the gas, we have attempted to constrain the post-shock electron temperature by fitting the spectrum of Region 3 in the energy range 1.5–3 keV, where the lines are weaker relative to the continuum. A 1.3 keV Gaussian line was included in this fit, as discussed in Section 3.2. Its energy and normalization were fixed by fitting it together with an APEC model over the energy range 0.5–2 keV. For the 1.5–3 keV fit, the abundances were fixed at 0.5 solar. The resulting 90 per cent confidence range for the temperature is 0.52–1.39 keV, consistent with the previous thermal fit.

If the flow time through Region 3 is comparable to or smaller than the electron-ion equilibration time, then the shocked protons there could be significantly hotter than the electrons (cf. Kraft et al. 2007a). In that case, the post-shock pressure may be significantly greater than estimated above, only providing a lower limit on the true pressure of the radio lobe. The value of the lobe pressure is important, since it determines the strength and speed of the shock, and the estimated jet power scales approximately as $P^{3/2}$, so this issue warrants careful scrutiny.

To determine how much the electron and proton temperatures may differ, we have used the two-fluid hydrodynamic model of Kraft et al. (2007a). Motivated by observations of Galactic SNRs, this model assumes that the protons are heated rapidly in a collisionless shock, while the electrons are heated by Coulomb collisions with the protons. The model is spherically symmetric and, for the cases illustrated here, the shock is driven by constant power input into an expanding 'radio lobe' at the centre of an initially uniform atmosphere. For scaling purposes, the shock radius is taken to be 1.6 kpc (90 arcsec).

In terms of the electron and proton temperatures, $T_{\rm e}$ and $T_{\rm p}$, respectively, the energy exchange can be expressed as $\mathrm{d}T_{\rm e}/\mathrm{d}t = \nu(T_{\rm p} - T_{\rm e})$, where the rate coefficient is determined chiefly by the electron temperature, approximately $\nu \propto n_{\rm e} T_{\rm e}^{-3/2}$ (e.g. Kraft et al. 2007a). Although the electron-ion equilibration time is relatively short, $\simeq 2 \times 10^5$ yr for $n_{\rm p} = 0.033$ cm^{-3} and $kT = 0.97$ keV, it is not much shorter than the sound crossing time of Region 3, $\simeq 2.6 \times 10^5$ yr. Increasing the temperature of the shocked gas increases the electron-proton equilibration time while also decreasing the sound crossing time. Thus, although electrons and protons in Region 3 should have much the same temperature if the electron temperature there is close to 1 keV, their temperatures can differ significantly if the electron temperature is moderately higher.

This is illustrated in Fig. 7, which shows post-shock proton and electron temperature profiles for two cases. In the first case [Fig. 7(a)], the emission measure weighted electron temperature in Region 3 (1.48–1.60 kpc) is 1 keV and the rms proton density is 0.033 cm^{-3}. In this case, the difference between the electron and proton temperatures is negligible. For the second case [Fig. 7(b)], the rms density is the same, but the emission measured weighted electron temperature is close to 1.4 keV, the 90 per cent level upper limit. Here, the proton temperature is $\sim$70 per cent greater than the electron temperature. The post-shock pressure would then be roughly 35 per cent larger than suggested by the electron temperature. This disparity between electron and proton temperatures grows rapidly with electron temperature. However, if the electron temperature is smaller than the 1.4 keV upper limit, our estimate

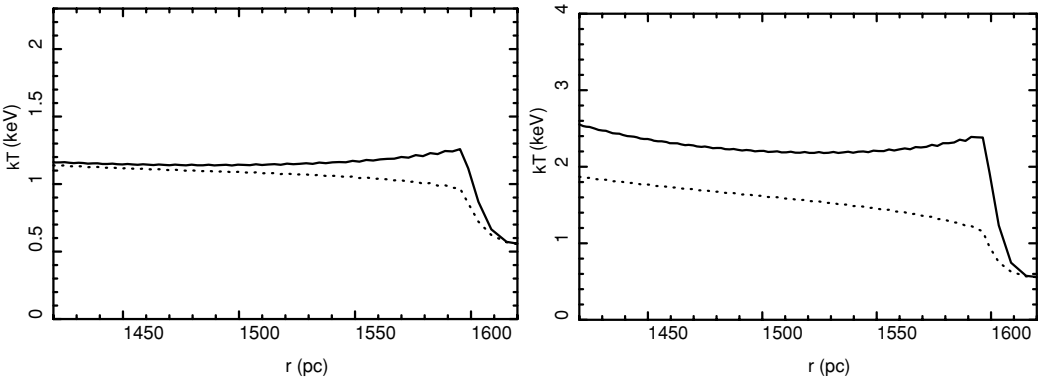

Figure 7. Post-shock proton temperature (solid line) and electron temperature (dotted line) profiles obtained from our two-fluid hydrodynamical modelling (Section 4.3) for $kT = 1$ keV (left-hand side) and $kT = 1.4$ keV (right-hand side).

for the post-shock pressure should be a reasonable estimate of the true pressure.

4.4 Implications of the X-ray synchrotron interpretation for particle acceleration at radio-lobe shocks

In Section 4.1, we demonstrated that a synchrotron origin for the shell X-ray emission is consistent with the broad-band SED of the shell emission in a region exterior to the radio lobe (where the most constraining radio limits could be obtained). We have also shown that the lack of thermal X-ray emission from the outer parts of the shell is consistent with the expected level of emission from a strong shock – the observed thermal X-ray emission in the more central north-west shell region (Section 3.2) and the lack of any signatures of such emission in its outer parts (Section 3.1) are as expected for a strong shock propagating into Cen A's environment. We conclude that the majority of the shell X-ray emission is synchrotron emission from high-energy particle acceleration at the shock front. Interestingly, the inferred expansion speed of the radio lobe at its outer edge, as calculated in the previous section, is very similar to the expansion speeds of SNRs that show X-ray synchrotron emission (e.g. Rothenflug et al. 2004; Warren et al. 2005; Vink et al. 2006; Acero, Ballet & Decourchelle 2007), whereas at the NW edge, where no significant non-thermal emission is detected (although particle acceleration to X-ray-emitting energies cannot be ruled out – see Section 4.1), the expansion speed is significantly lower. If the inner lobes of Cen A are indeed expanding at these high velocities, then it is perhaps not unexpected to see such a strong signature of high-energy particle acceleration.

The statistically significant decrease in spectral index in the outer ∼50 arcsec of the shell (Section 3.3) could indicate differences in the particle acceleration behaviour as a function of distance and hence of shock expansion velocity. A possible interpretation is that the spectrum is flattest at the outermost edge of the shell (where the expansion speed is highest) because of a higher value for $\gamma_{\rm max}$, the observed high-energy cut-off of the electron population, with the high-energy cut-off moving to lower energies, thus steepening the spectrum, in regions closer to the nucleus where the shock front is slower due to a denser environment. This would require $\gamma_{\rm max}$ in the range 10^7–10^9 over the bright shell region, and significantly lower than 7×10^7 in Region 3. (We note that, assuming the observed value of $\gamma_{\rm max}$ is determined by radiative losses, the high-energy cut-off for hadrons would be significantly higher). If the X-ray-emitting electrons are being accelerated by diffusive shock acceleration, and if the high-energy cut-off is determined by the synchrotron loss time-scale, then we can determine the dependence of $\gamma_{\rm max}$ on shock speed, as well as the expected value of $\gamma_{\rm max}$ for the shock conditions we observe. The high-energy cut-off for particle acceleration has been discussed extensively in the context of X-ray synchrotron emission from SNRs (e.g. Lagage & Cesarsky 1983; Reynolds 1996). For electrons, the acceleration time-scale to a given energy E depends on B_1 (the pre-shock magnetic field strength), $E, v_{\rm shock}$, the ratio of the electron mean free path along the magnetic field to the gyroradius (f, assumed to between 1 and ∼10), and on a factor R_J that takes into account the decrease in efficiency of scattering if the magnetic field direction is not parallel to the shock. We used equation (1) of Reynolds (1996),

$$E_{\rm max} \approx 0.1(fR_JB_1)^{-1/2}v_8 \quad \text{erg}, \tag{1}$$

where units are cgs and the shock speed is in units of $10^8\,{\rm cm\,s^{-1}}$. We assumed $f = 10$, $R_J = 1$ and $B_1 = 1\,\mu$G, and find that $\gamma_{\rm max} \sim 10^8$ for the outer edge of the shell and $\sim 3 \times 10^7$ at Region 3. In order to fit a synchrotron model consistent with the observed X-ray spectral index for Region 2, and with equipartition B fields, we require $\gamma_{\rm max}$ in the range 2×10^8–4×10^8 (see Fig. 6), which is roughly consistent with this analysis. This suggests that a model in which the observed X-ray spectral changes can be explained by changes in $\gamma_{\rm max}$ as a function of shock speed is viable. We have not considered the role of changes in B_1 and f along the shell in this discussion – these are likely to vary somewhat with position as well, but the dependence of $\gamma_{\rm max}$ on these parameters is weaker so that the change is shock speed is likely to be the dominant effect.

4.5 Implications for large-scale shocks in other galaxies

If we accept a synchrotron origin for the X-ray emission from Cen A, then the X-ray properties of the outer shell region cannot be used to measure the impact of the radio galaxy on its environment directly; however, the detection of thermal emission from the shocked gas in Region 2 allows us to infer the dynamics of the shocked shell and radio lobe indirectly as discussed above. The results on the overall dynamics of the radio lobe and its environmental impact are not significantly different from the conclusions of Kraft et al. (2003). Unlike the shock in Cen A, the strong shock detected in the similar system NGC 3801 (Croston et al. 2007) is clearly dominated by thermal X-ray emission, with no significant X-ray synchrotron emission. It is likely that the lobes of NGC 3801 are expanding much more slowly than the outer parts of Cen A (∼750 km s^{-1}, similar to Cen A's expansion speed at Region 3), and so the lack of strong high-energy particle acceleration in that system is probably explained by this lower speed.

The bolometric X-ray luminosity of the shell emission in Cen A is $\sim 4 \times 10^{39}$ erg s^{-1}, and so shocks on similar physical scales will be undetectable in more distant radio galaxies; however, these results could also have implications for powerful FR II radio galaxies, whose lobes are much larger. A number of nearby FR II radio galaxies have been found to reside in comparatively gas poor environments (e.g. Kraft et al. 2005, 2007b), and so may be having similarly dramatic effects on their environments. If supersonic expansion is occurring in FR IIs at speeds similar to that of Cen A, then high-energy particle acceleration could be important in FR II environments. We considered the example of the nearby FR II radio galaxy 3C 33, whose poor environment is discussed in Kraft et al. (2007b). If the lobes of 3C 33 are expanding at a similar speed to those of Cen A, and we assume (i) that the particle acceleration is similarly efficient and (ii) that the density of accelerated particles is proportional to the density of the shocked gas, then the expected X-ray synchrotron flux should scale as $S \propto n_{\rm ism} V D_L^{-2}$. The external density ratio $n_{\rm 3C33}/n_{\rm CenA}$ is $\sim$0.01, the volume ratio is $\sim$7500, and the square of the ratio of luminosity distances is 1.9×10^{-4}, giving an expected reduction in X-ray flux of a factor of $\sim$70 and a predicted 1-keV flux density from synchrotron emission of $\sim$1 nJy. This is comparable to the level of non-thermal X-ray emission measured by Kraft et al. and attributed to IC scattering of the CMB (e.g. Croston et al. 2005), and so for 3C 33 the observed X-ray flux levels from the radio lobes do not rule out the possibility that high-energy particle acceleration is occurring at a similar level to Cen A. However, the spectral index for the non-thermal X-ray emission from 3C 33 and other FR II radio lobes ($\sim$1.5– 1.7) is flatter than that of the shell in Cen A, and no edge-brightening is observed for the X-ray lobes of FR IIs (Croston et al. 2005). In addition, the X-ray flux from this process decreases as $(1 + z)^4$, unlike the IC/CMB flux, and so IC/CMB is predicted to dominate by a large factor in the majority of FR IIs, which are more distant than 3C 33. Nevertheless, it is plausible that particle acceleration by expanding FR II lobes may result in significant cosmic ray populations and potentially detectable X-ray synchrotron emission for sources in weaker environments.

4.6 Implications for Cen A as a cosmic ray source

It is interesting to consider the implications of these results for our understanding of Cen A as a source of cosmic rays, particularly in light of recent results from the Pierre Auger Observatory showing an overdensity of UHECRs from the direction of Cen A (Abraham et al. 2007; Moskalenko et al. 2008), which had been predicted previously (Romero et al. 1996). To have efficient cosmic-ray acceleration to high energies, the particle gyroradius cannot be significantly larger than the size of the acceleration region. By the criterion of Hillas (1984), for an assumed acceleration region of $\sim$300 pc (the observed thickness of the shock front: Section 4.2) and $B = 7$ μG, typical particle energies cannot exceed $\sim 2 \times 10^{18}$ eV. Hence, magnetic fields significantly higher than equipartition (e.g. $\sim$400 μG) would be required for the shock front to accelerate cosmic rays to 10^{20} eV. There is considerable evidence that magnetic fields can be amplified by large factors at the forward shocks of SNRs (e.g. Berezhko & Völk 2004; Ellison, Decourchelle & Ballet 2004) (e.g. lower limits on B in Cass A are of the order of those required here to confine cosmic rays of 10^{20} eV; Vink & Laming 2003), and so if similar processes were operating at the Cen A shock front then UHECR energies could be achieved. However, the equipartition magnetic field strengths in SNRs are comparable to values inferred from the thickness of the shock front. This suggests that magnetic field amplification by similar factors at the Cen A shock may be unlikely, as it would require a large departure from equipartition in the direction of magnetic field dominance. The Cen A shock front appears resolved in our *Chandra* observations, with a width of $\sim$2 arcsec (corresponding to $\sim$35 pc). We can use the shock thickness to estimate the magnetic field strength in the shell, assuming it is determined by synchrotron losses. Following the method used by Vink & Laming (2003) for the Cas A SNR, assuming the accelerated electrons travel away from the shock front with the shocked gas at a speed of $0.25 v_{\rm shock}$, we find synchrotron lifetimes of $\sim 5 \times 10^4$ yr are required. These lifetimes for photons emitting at 1 keV imply magnetic field strengths of $\sim$1 μG, consistent with the equipartition values discussed above, but much lower than would be required to accelerate UHECRs. In addition, as discussed above, our X-ray observations suggest that we may be observing the high-energy cut-off in the electron distribution directly, at energies of $\sim \gamma = 10^7 - 10^8$, which corresponds to electron energies of $\sim 10^{14}$ eV. Nevertheless, if the cut-off energy is determined by losses then its value will be higher for hadrons. We conclude that it is possible that the Cen A shock could accelerate cosmic rays to UHECR energies; however, this would require magnetic field amplification by large factors, and magnetic domination of the energetics of the synchrotron-emitting plasma. The $\sim$600-kpc-scale giant outer lobes of Cen A may be a more likely candidate for the origin of the UHECRs apparently associated with Cen A (e.g. Hardcastle et al. 2008; Moskalenko et al. 2008).

4.7 Implications for Cen A as a TeV source

It is also important to consider the implications of our results for emission at higher energies. The detection of X-ray synchrotron emission from the shell implies the existence of electrons with TeV energies (for plausible values of B), and hence it is possible that the shock could produce significant emission at very high energies. We therefore investigated the predicted IC emission from the Cen A shell. The dominant photon fields in the shell region that can be scattered to gamma-ray energies are (1) starlight from the host galaxy, and (2) the CMB. We determined the photon density from starlight at the position of the shell by deprojecting the V-band surface brightness profile of van den Bergh (1976), using the method of Mellier & Mathez (1987) to obtain a V-band spectral energy density at a radius of 268 arcsec (midway between the inner and outer radii encompassing Region 1) of 1.6×10^{-28} J Hz^{-1} m^{-3}. A spectral energy distribution for the entire galaxy was obtained using the UV measurements of Welch (1979), optical measurements from de Vaucouleurs et al. (1991), IR measurements from Two Micron All Sky Survey (Jarrett et al. 2003) and *IRAS* (Golombek, Miley & Neugebauer 1988), which was normalised to the V-band energy density given above. We note that the corresponding total energy density at the radius of interest is in good agreement with that determined by Stawarz et al. (2006). The analysis was carried out for Region 1, so as to include most of the X-ray-emitting electrons, and the electron population was modelled as described in Fig. 4.1. We used the SYNCH code of Hardcastle, Birkinshaw & Worrall (1998) to determine the predicted IC emission from starlight and IC/CMB. Fig. 8 shows the IC predictions for magnetic field strengths of 1 μG (the value obtained above from consideration of the width of the X-ray shell) and 7 μG (the equipartition value for Region 2 discussed in Section 4.1). Also plotted is an upper limit from the high-energy stereoscopic system (HESS) of $<5.68 \times 10^{-12}$ ph cm^{-2} s^{-1} above 0.19 TeV (Aharonian et al. 2005), which corresponds to a flux density at 0.19 GeV of 3.8×10^{-15} Jy for an assumed photon

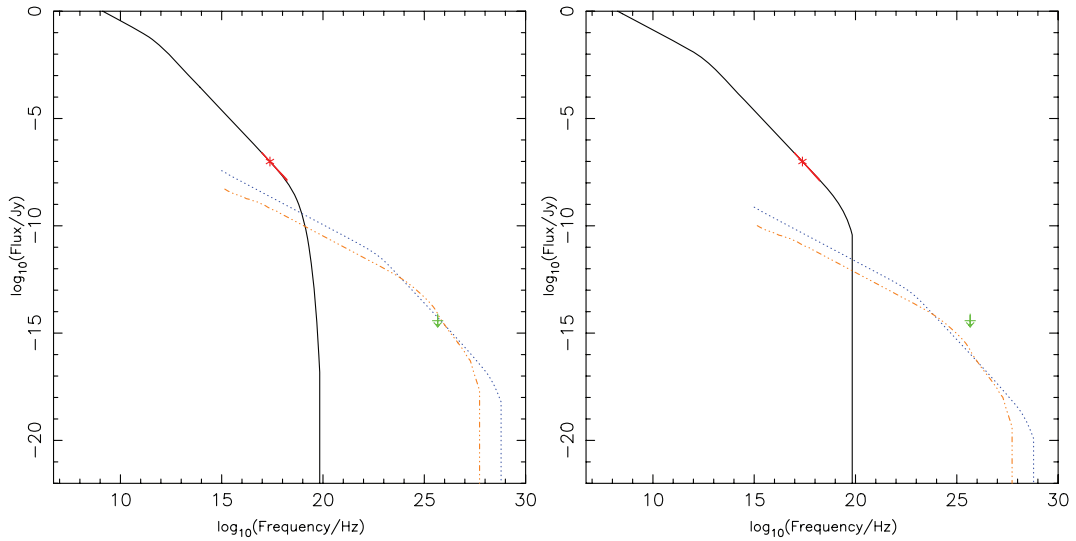

Figure 8. Predictions for IC emission from the SW shell of Cen A from scattering of starlight (orange dash–dotted line) and the CMB (blue dotted line). The electron distribution is as in the left-hand panel of Fig. 6 for $B = 1$ μG (left-hand side) and 7 μG (right-hand side). The star indicates the measured X-ray flux density, and the upper limit is the HESS measurement of Aharonian et al. (2005).

index of 2.0, consistent with our assumed spectrum. For $B = 7$ μG, we predict a total flux density at 0.19 GeV from IC scattering of starlight and the CMB of 3.2×10^{-16} Jy, an order of magnitude below the HESS limit, which corresponds to $F(> 0.19\,\mathrm{GeV}) \sim 2 \times 10^{-13}$ photons cm^{-2} s^{-1} above 0.19 TeV (for $\Gamma = 2$). However, with a lower magnetic field strength, as is suggested by the calculation in Section 4.6, we find a predicted total flux density at 0.19 GeV of 1.6×10^{-14} Jy, corresponding to a total $F(> 0.19\,\mathrm{GeV}) \sim 2 \times 10^{-11}$ ph cm^{-2} s^{-1}, that is we predict a flux that is comparable to or higher than the HESS upper limit. Hence, it is reasonable to think that a TeV detection of the Cen A shell may be possible with deeper observations. It is unclear whether the Cen A shell would be expected to dominate over emission from the jet (which also contains electrons of TeV energies; e.g. Hardcastle et al. 2007) at TeV energies. A full calculation of the predicted TeV emission from the jet is beyond the scope of this paper; however, a rough estimate based on the X-ray jet properties discussed in Hardcastle et al. (2007) suggests a level of TeV emission comparable to that from the shell. In principle, it would be possible to distinguish spectrally between IC emission from the jet and the shell, as the diffuse X-ray synchrotron emission in the jet has a significantly steeper spectral index than the shell. Hence, deeper TeV observations of Cen A have the potential to provide important constraints on the properties of the fluid in the shocked shell as well as the jet. We note that Cen A has now been detected at GeV energies by Fermi (Abdo et al. 2009) at level significantly higher than predicted by the IC models in Fig. 8. It is likely that the Fermi source is dominated by emission from the nucleus or inner jets (see also Orellana & Romero 2009).

5 CONCLUSIONS

We have presented a detailed study of the X-ray emission associated with the south-west inner lobe of Cen A. Our deep observations as part of a *Chandra* Very Large Programme have enabled us to establish firmly that the majority of the X-ray emission associated with the shock surrounding the SW lobe, first discussed by Kraft et al. (2003), is X-ray synchrotron emission associated with particle acceleration at the shock front, and not thermal emission from shocked gas. We have investigated the spectral structure of the X-ray shell, presenting maps of spectral structure for the first time, and we conclude that non-thermal emission dominates over most of the shell, except in the inner regions, where the thermal X-ray emission can be used to determine the shock conditions. We have described a self-consistent model for the lobe and shock dynamics, considering in detail the implications of possible electron-ion non-equilibrium in the shocked material. Our analysis of the spatial distribution of power-law spectral index constrains $\gamma_{\max}$ for the accelerated particles to be $\sim 10^8$ at the strongest part of the shock, consistent with the expectations of diffusive shock acceleration theory. We considered the implications of our results for Cen A's role as a source of cosmic rays, but conclude that the inner lobe shocks are unlikely to be an important source of UHECRs as this would require very high magnetic field strengths. Finally, we considered the expected IC emission from this synchrotron shell, finding that the predicted emission from IC scattering of starlight and the CMB is comparable to current upper limits at TeV energies.

ACKNOWLEDGMENTS

This work was partially supported by NASA grants NAS8-03060 and GO7-8105X, and Hubble grant HST-GO-10597.03-A. We gratefully acknowledge support from the Royal Society (research fellowship for MJH).

REFERENCES

Abdo A. A. et al., 2009, ApJ, submitted (arXiv:0902.1559)
Abraham J. et al., [for the Pierre Auger Collaboration], 2007, Sci, 318, 938
Acero F., Ballet J., Decourchelle A., 2007, A&A, 475, 883
Aharonian F. et al. [for the HESS collaboration], 2005, A&A, 441, 465
Berezhko E. G., Völk H. J., 2004, A&A, 419, 27
Brookes M. H., Lawrence C. R., Keene J., Stern D., Gorijan V., Werner M., Charmandaris V., 2006, ApJ, 646, 41
Buote D. A., 2000, MNRAS, 311, 176
Croston J. H., Hardcastle M. J., Harris D. E., Belsole E., Birkinshaw M., Worrall D. M., 2005, ApJ, 626, 733
Croston J. H., Kraft R. P., Hardcastle M. J., 2007, MNRAS, 660, 191
Croston J. H., Hardcastle M. J., Birkinshaw M., Worrall D. M., Laing R. A., 2008, MNRAS, 386, 1709

David L. P., Jones C., Forman W., Vargas I. M., Nulsen P., 2006, ApJ, 653, 207
de Vaucouleurs G., de Vaucouleurs A., Corwin H. G., Jr, Buta R. J., Paturel G., Fouque P., 1991, Third Reference Catalogue of Bright Galaxies. Springer-Verlag, Berlin
Dickey J. M., Lockman F. J., 1990, ARA&A, 28, 215
Dyer K. K., Reynolds S. P., Borkowski K. J., 2004, ApJ, 600, 752
Ellison D. C., Decourchelle E., Ballet J., 2004, A&A, 413, 189
Evans D. A., Kraft R. P., Worrall D. M., Hardcastle M. J., Jones C., Forman W. R., Murray S. S., 2004, ApJ, 612, 786
Fabian A. C., Sanders J. S., Allen S. W., Crawford C. S., Iwasawa , Johnstone R. M., Schmidt R. W., Taylor G. B., 2003, MNRAS, 344, L43
Fabian A. C., Sanders J. S., Taylor G. B., Allen S. W., Crawford C. S., Johnstone R. M., Iwasawa K., 2006, MNRAS, 366, 417
Ferrarase L., Mould J. R., Stetson P. B., Tonry J. L., Blakeslee J. P., Ajhar E. A., 2007, ApJ, 654, 186
Forman W. et al., 2005, ApJ, 635, 894
Golombek D., Miley G. K., Neugebauer G., 1988, AJ, 95, 26
Hardcastle M. J., Birkinshaw M., Worrall D. M., 1998, MNRAS, 294, 615
Hardcastle M. J., Kraft R. P., Worrall D. M., 2006, MNRAS, 368, L15
Hardcastle M. J. et al., 2007, ApJ, 670, 81
Hardcastle M. J., Cheung C. C., Feain I. J., Stawarz Ł., 2008, MNRAS, 393, 1041
Hillas A. M., 1984, ARA&A, 22, 425
Jarrett T. H., Chester T., Cutri R., Schneider S. E., Huchra J. P., 2003, ApJ, 125, 525
Jetha N. N., Hardcastle M. J., Ponman T. J., Sakelliou I., 2008, MNRAS, 391, 1052
Jordán A. et al., 2007, ApJ, 671 117
Kraft R. P., Vázquez S. E., Forman W. R., Jones C., Murray S. S., Hardcastle M. J., Worrall D. M., Churazov E., 2003, ApJ, 592, 129
Kraft R. P., Hardcastle M. J., Worrall D. M., Murray S. S., 2005, ApJ, 622, 149
Kraft R. P. et al., 2007a, ApJ, 665, 1129
Kraft R. P., Birkinshaw M., Hardcastle M. J., Evans D. A., Croston J. H., Worrall D. M., Murray S. S., 2007b, ApJ, 659, 1008
Kraft R. P. et al., 2008, ApJ, 677, 97
Lagage P. O., Cesarsky C. J., 1983, A&A, 125, 249
Mellier Y., Mathez G., 1987, A&A, 175, 1
Moskalenko I. V., Stawarz, Ł., Porter T. A., Cheung C. C., 2008, ApJ, 693, 1261
Neff A. G., Schiminovich D., Martin C. D., 2003, A&AS, 203, 9607
Orellana M., Romero G. E., 2009, MNRAS, submitted (arXiv:0902.0731)
Reynolds S. P., 1996, ApJ, 459, 13
Rho J., Reynolds S. P., Reach W. T., Jarrett T. H., Allen G. E., Wilson J. C., 2003, ApJ, 592, 299
Romero G. E., Combi J. A., Perez Bergliaffa S. E., Anchordoqui L. A., 1996, Astropart. Phys., 5, 279
Rothenflug R., Ballet J., Dubner G., Giacani E., Decourchelle A., Ferrando P., 2004, A&A, 425, 121
Sivakoff G. R. et al., 2008, ApJ, 677, 27
Smith R. K., Brickhouse N. S., Liedahl D. A., Raymond J. C., 2001, ApJ, 556, 91
Stawarz, Ł., Aharonian F., Wagner S., Ostrowski M., 2006, MNRAS, 371, 1705
van den Bergh S., 1976, ApJ, 208, 673
Vink J., Laming M. J., 2003, ApJ, 584, 758
Vink J., Bleeker J., van der Heyden K., Bykov A., Bamba A., Yamazaki R., 2006, ApJ, 648, 33
Warren J. S., 2005, ApJ, 634, 376
Welch G. A., 1979, ApJ, 228, 419
Worrall D. M. et al., 2008, ApJ, 673, 135

This paper has been typeset from a TEX/LATEX file prepared by the author.